AGU PUBLICATIONS

Geophysical Research Letters

RESEARCH LETTER
10.1002/2015GL063224

Key Points:
- A multiple-flyby mission to Europa can recover key geophysical parameters
- Laser altimetry can uniquely and accurately recover the global shape of Europa
- Laser altimetry enables the recovery of h2 to constrain the ice shell thickness

Supporting Information:
- Figure S1

Correspondence to:
E. Mazarico,
erwan.m.mazarico@nasa.gov

Citation:
Mazarico, E., A. Genova, G. A. Neumann, D. E. Smith, and M. T. Zuber (2015), Simulated recovery of Europa's global shape and tidal Love numbers from altimetry and radio tracking during a dedicated flyby tour, *Geophys. Res. Lett.*, *42*, 3166–3173, doi:10.1002/2015GL063224.

Received 25 JAN 2015
Accepted 7 APR 2015
Accepted article online 10 APR 2015
Published online 7 MAY 2015

Simulated recovery of Europa's global shape and tidal Love numbers from altimetry and radio tracking during a dedicated flyby tour

Erwan Mazarico[1], Antonio Genova[1,2], Gregory A. Neumann[1], David E. Smith[2], and Maria T. Zuber[2]

[1]Planetary Geodynamics Laboratory, NASA Goddard Space Flight Center, Greenbelt, Maryland, USA, [2]Department of Earth, Atmospheric and Planetary Sciences, Massachusetts Institute of Technology, Cambridge, Massachusetts, USA

Abstract The fundamental scientific objectives for future spacecraft exploration of Jupiter's moon Europa include confirmation of the existence of subsurface ocean beneath the surface ice shell and constraints on the physical properties of the ocean. Here we conduct a comprehensive simulation of a multiple-flyby mission. We demonstrate that radio tracking data can provide an estimate of the gravitational tidal Love number k_2 with sufficient precision to confirm the presence of a liquid layer. We further show that a capable long-range laser altimeter can improve determination of the spacecraft position, improve the k_2 determination ($<$1% error), and enable the estimation of the planetary shape and Love number h_2 (3–4% error), which is directly related to the amplitude of the surface tidal deformation. These measurements, in addition to the global shape accurately constrained by the long altimetric profiles, can yield further constraints on the interior structure of Europa.

1. Background and Motivation

Despite the high-radiation environment of Jupiter's radiation belts, its moon Europa is one of the Solar System bodies with greatest potential for life, due to the presence of a subsurface ocean, nutrient exchange with the silicate mantle on its floor, and an energy source in the form of tidal heating. Dedicated exploration remains a high priority for the scientific community [*National Research Council*, 2011]. The thickness of the moon's ice shell is critical with regard to understanding the possible exchange of material between the ocean and surface, and the scientific potential of future lander exploration. Both the long-wavelength shape of Europa and its tidal response to Jupiter's time-variable gravitational forcing can help address this geophysical objective.

After the release of the Planetary Science Decadal Survey, various mission architectures were studied, including a multiple-flyby scenario. Because this concept did not include a laser altimeter, key geophysical parameters would not be measured, in particular the global shape and the surface tidal deformation. The lack of these measurements would make the characterization of the ice shell thickness difficult, because of the large trade-off between thickness and viscosity of the ice [*Wahr et al.*, 2006].

Analogous to the Galileo and Cassini missions, the spacecraft would conduct a series of flybys over the course of several years while in orbit around Jupiter, but with an almost exclusive focus on Europa. We used the notional trajectory 13F7-A21 developed by the Europa Pre-Project, optimized for spatial and phase coverage and surface illumination. It consists of 45 flybys between March 2029 and October 2031. We assumed that medium-gain antennas allow continuous tracking from Earth via the Deep Space Network when in proximity of Europa, and that the spacecraft is tracked in X band (~8 GHz) over the 4 h surrounding the closest approach, in addition to the typical 8 h long daily tracking passes. The plasma noise is the main contributor to the radio error budget, and we compute the observation noise level at 60 s sampling from the Sun-Probe-Earth angle of each flyby, following *Iess et al.* [2014]. The radio data are thus significantly degraded for some flybys (e.g., #39 in June 2031).

Park et al. [2011] used an earlier version of the Europa flyby tour trajectory to perform a simulation through covariance analysis to assess the recoverability of Europa's tidal Love number k_2. They found that a higher frequency Ka band (~32 GHz) system could yield an uncertainty of ~10% (0.05), sufficient to detect the presence of a subsurface ocean. In this work, we performed a comprehensive simulation

of the complete Europa Clipper flyby tour with both radiometric and altimetric measurements, in an attempt to retrieve more key geophysical parameters, in particular the surface displacements not detectable by gravity alone. With six flybys by Cassini, *Iess et al*. [2012] recovered the tidal Love number for Titan to ~12% accuracy.

This paper is organized as follows. Section 2 details the assumptions about the laser altimeter, the altimetric data quality, and sampling used in the simulation. Section 3 describes the simulation setup, including our methods, assumptions for a priori models, and initial errors, as well as the data coverage and noise sources. In sections 4 and 5, we present the results of a covariance analysis and the full simulation, respectively. Our results quantitatively demonstrate the quality of the recovery of the long-wavelength shape from altimetry and that of the low-degree gravity and Love number parameters from combined radio tracking and altimetric crossovers.

2. Laster Altimeter

2.1. Instrument Description

Laser altimeters measure topography with high accuracy from the time of flight of a short laser pulse reflected on the surface. These ranges are also strong geodetic constraints when used in Precise Orbit Determination (POD). Like other types of active instruments, laser altimeters have a maximum operating range (typically $<$400 km) and thus have generally been limited to orbital missions [*Smith et al*., 1997, 2001; *Zuber et al*., 1997; *Araki et al*., 2009; *Smith et al*., 2010]. The Mercury Laser Altimeter (MLA) detected ground returns up to ~1800 km altitude [*Zuber et al*., 2012] in a highly eccentric orbit and was the basis for the instrument concept for the simulation.

The simulated altimeter is a high-performance and flexible instrument that can operate at variable pulse energy and firing frequency to best match the changing observation geometry over the course of a flyby. Operations would start at $>$4500 km with 8 Hz pulses, which dramatically improves the spatial coverage in terms of both quantity and uniformity (Figure 1a). A typical flyby yields ~100,000 altimetric returns over a $>$150° long arc. The precise determination of the gravity field by radio tracking and of the shape of Europa by an altimeter can place constraints on the ice shell compensation and thickness variations [*Nimmo et al*., 2007, 2011; *Mitri et al*., 2014] but also support the calibration of camera images and stereographic reconstructions [*Preusker et al*., 2011; *Scholten et al*., 2012].

The operating frequency is increased as needed to obtain the highest number of ground returns, from 8 Hz at ~4500 km range up to a maximum frequency of 128 Hz below ~1000 km altitude. As shown in Figure 1b, the spot size increases and the ground speed decreases with altitude, resulting in nearly contiguous spots for the majority of the flyby duration, thanks to the variable operating laser firing frequency. Even at closest approach, typically 100 km, the spots (~10 m) are separated by only small gaps (~20 m). Except in specific locations within chaos-like regions ($<$20% surface area) [*Figueredo and Greeley*, 2003] where extreme slopes can occur, this sampling is sufficient to prevent significant interpolation errors compared to the tidal signal amplitude (~30 m) [*Sotin et al*., 2009]. Indeed, with a maximum typical root-mean-square (RMS) surface slope of 10°, the worst-case interpolation error is ~80 cm, which is of the same order as the measurement noise ($<$1 m including detector response and timing error, similar to MLA at long range) [*Zuber et al*., 2012]. With large spot sizes, the range can be somewhat biased by the spot-scale slopes; this effect is on the order of a few meters at most, but is partially compensated by the smoother topography sampled over larger length scales, due to the fractal nature of planetary surface topography. The reconstructed pointing knowledge of the spacecraft is assumed to be the same as the beam divergence of the laser, 100 μrad.

2.2. Shape Recovery

The geodetic accuracy of the laser altimetric ranges yields the global shape of Europa. The long-range capability is especially important as it provides near-global coverage with few regional gaps (Figure 1a). In order to illustrate the quality of the recovery of the low-degree shape, we performed constrained inversions to estimate the spherical harmonics coefficients that describe the global shape to degree 32 (spatial block size ~150 km), given a topographic model and the ground tracks of the notional Europa Clipper mission. We used several a priori shapes (Figure S1).

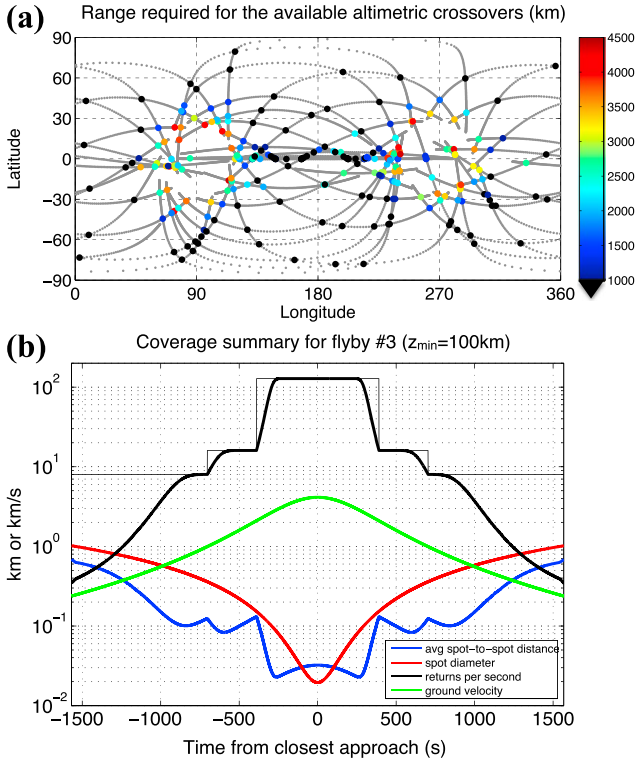

Figure 1. (a) Spacecraft ground tracks (up to an altitude of 4500 km; sampled every 10 s) and the resulting crossover locations. Color indicates the altitude of the higher of the two intersecting tracks (in km) and highlights that the 90°/270° regions are not well sampled with a <1000 km range capability. (b) Key parameters during a typical flyby (~100 km closest approach). The commanded firing frequency of the instrument (thin) and the effective measurement rate (thick) are in black. As the spacecraft approaches Europa, its ground speed (green) increases and the laser footprint shrinks (red). Given the measurement rate, the average spot-to-spot distance (blue) can be computed. During the majority of the flyby, the spots are overlapping or near contiguous (i.e., the red curve is above the blue one).

Table 1 shows that the coverage obtained by the altimeter yields substantial improvements over what a shorter-range instrument operating between 400 and 1000 km could achieve (Figure S1). The C_{20}, C_{22}, and S_{22} shape coefficients define the flattening, equatorial ellipticity, and orientation, improve by a factor of 5–10 due to the longer ground tracks. In combination with the low-degree gravity coefficients, the determination of the low-degree shape to high accuracy enables several types of studies, such as its orientation with respect to the (gravitational) figure, the degree of compensation in the ice shell [*Ojakangas and Stevenson*, 1989; *Hemingway et al.*, 2013; *Mitri et al.*, 2014; *Lefèvre et al.*, 2014], and indirect constraint on the heat flow. For example, the degree 4 terms, also well determined with the greater altimeter coverage, are important because they are not expected to arise from tidal or rotational effects but could be large depending on the heat loss mechanism of the ice shell (conductive versus convective) [*Nimmo et al.*, 2007].

3. Simulation Setup

We use the NASA Goddard Space Flight Center's GEODYN II orbit determination and geodetic parameter estimation software, which has been used for geophysical studies on numerous spacecraft missions [e.g., *Lemoine et al.*, 1997, 2001, 2013; *Mazarico et al.*, 2014]. Detailed force and measurement models are used to iteratively integrate the spacecraft trajectory and minimize the difference between the computed and measured observables [cf. *Lemoine et al.*, 2013], a process called Precise Orbit Determination (POD). *Lemoine et al.* [2001] describe the altimetric crossover measurement type and its use with Mars Orbiter Laser Altimeter [*Zuber et al.*, 1992] data for POD of the Mars Global Surveyor spacecraft. For each of the 45 flybys, we focused on 24 h centered on the closest approach. The integration of the spacecraft trajectory is initiated ~200,000 km away from Europa, outside of its sphere of influence.

To construct the truth gravity field, we combined the degree 2 gravity spherical harmonics of Europa [*Anderson et al.*, 1998], the degrees 3 and 4 from estimates of Titan's [*Iess et al.*, 2010], and the higher degrees (to 50) from a Mars field [*Konopliv et al.*, 2011] scaled appropriately to simulate the silicate mantle contribution [*Pauer et al.*, 2010]. The tidal parameters are $k_2 = 0.257$ and $h_2 = 1.20$, which translate to ~30 m radial tidal deformation and ~35 km ice thickness [*Wahr et al.*, 2006].

A 20 km wide 20 m/pixel stereo-derived digital elevation model (DEM) of Europa in a ridged plains region imaged by Galileo during the E4 flyby [*Head et al.*, 1999; *Nimmo and Schenk*, 2008] was used as representative of the global surface topography (Figure 2a). We added short-wavelength fractal noise to obtain a topography model of higher resolution, commensurate with the smallest altimeter footprints

Table 1. Values and Errors (in m) of the C_{20}, C_{22}, S_{22}, and C_{40} Spherical Harmonics Coefficients Recovered From Various A Priori Shapes With Different Ground Track Coverages[a]

		Truth	$z < 4500$ km			400 km $< z <$ 1000 km		
		Value	Value	Error		Value	Error	
Shape	C_{lm} or S_{lm}	(m)	(m)	(m)	(%)	(m)	(m)	(%)
Moon	C_{20}	−668.55	−651.63	16.92	2.5	−524.16	144.39	21.6
	C_{22}	109.63	141.25	31.62	28.8	287.3	177.67	162.1
	S_{22}	383.11	374.8	8.31	2.2	360.19	22.92	6.0
	C_{40}	215.89	239.43	23.54	10.9	70.15	145.74	67.5
Hydrostatic shape based on rescaled Mimas	C_{20}	−278.48	−278.31	0.17	0.1	−257.94	20.54	7.4
	C_{22}	−83.69	−82.61	1.08	1.3	−67.46	16.23	19.4
	S_{22}	−0.74	3.55	4.29	*579.7*	1.57	2.31	*312.2*
	C_{40}	13.87	16.94	3.07	22.1	10.7	3.17	22.9
Nimmo et al. [2007]	C_{20}	−45	−44.51	0.49	1.1	−26.73	18.27	40.6
	C_{22}	−103.32	−102.77	0.55	0.5	-86.79	16.53	16.0
	S_{22}	0	0.17	0.17	-	0.86	0.86	-
	C_{40}	21	20.63	0.37	1.8	12.5	8.50	40.5

[a]Maps of the a priori and recovered degree 10 expansions are shown in Figure S1. Numbers in italics are large due to the small a priori values.

(10 m/pixel). The RMS of these short-wavelength and midwavelength perturbations is 5 and 50 m, respectively, which produces a realistic slope distribution [*Schenk*, 2009].

To ensure the robustness of the simulation results, we strongly perturbed the truth parameters. Because we found that degree 4 coefficients are not well determined with the flyby geometry (signal-to-noise ratio ~ 1), we only adjusted the coefficients of degrees 2 and 3, which introduces realistic omission error. The imposed initial error on the C_{20} and C_{22} coefficients is 10 times the uncertainty given by *Anderson et al.* [1998], while the other coefficients are initially zero. The initial k_2 and h_2 are 0.107 (~60% error) and 0.60 (50% error), respectively. The scale factor for the solar radiation (modeled with a plate model of the spacecraft and nadir orientation) is perturbed by 20% but held fixed because of high correlation with the state. Future simulation efforts will include the perturbing effects of the Radioisotope Thermoelectric Generators or of

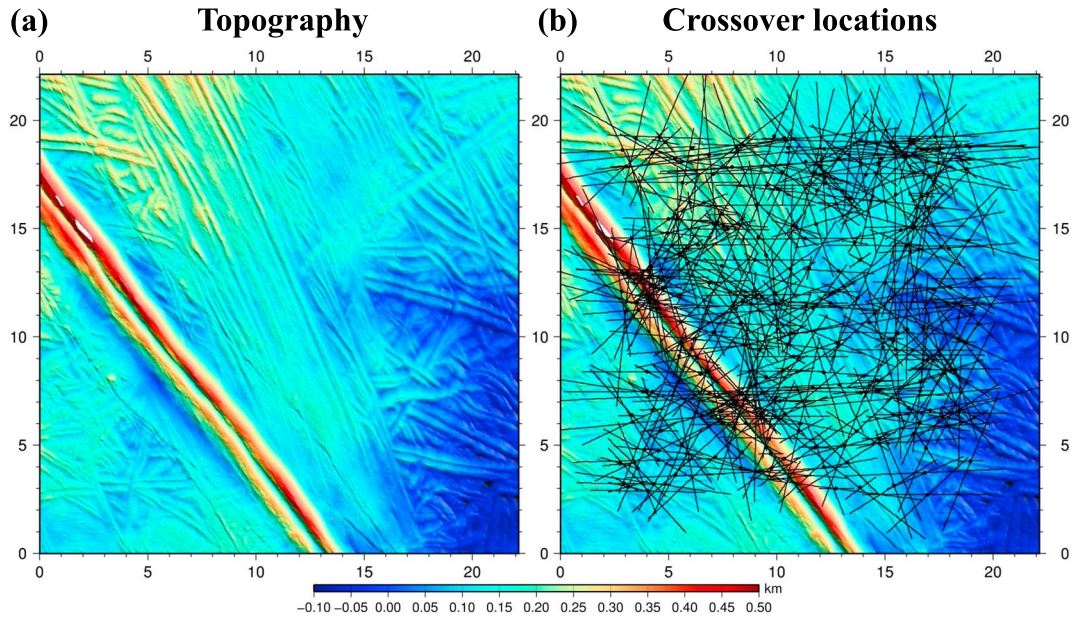

Figure 2. (a) Typical Europa topography used to compute the artificial altimetric ranges around the times of crossovers. (b) To capture some of the variability in terrain around Europa, each crossover center was randomly placed in the DEM, as indicated by the black dots and intersecting short segments. Axes are in kilometers.

Table 2. Values and Errors of the Tidal Love Numbers and Gravity C_{20}, C_{22}, S_{22}, and C_{30} Spherical Harmonics Coefficients Recovered From the Various Simulation Cases

	Truth	Covariance Analysis			Radio Only			Radio + Altimetry		
	Value	Value	Error	(%)	Value	Error	(%)	Value	Error	(%)
k_2	0.257	0.2572	0.0002	0.08	0.2495	0.0075	2.93	0.2546	0.0024	0.94
h_2	1.2	1.182	0.018	1.50	-	-	-	1.1660	0.0340	2.83
C_{20}	−4.3550E-04	−4.3547E-04	3.0000E-08	0.01	−4.3707E-04	1.5675E-06	0.36	−4.3672E-04	1.2165E-06	0.28
C_{22}	1.3100E-04	1.3097E-04	3.0000E-08	0.02	1.3228E-04	1.2831E-06	0.98	1.3158E-04	5.7729E-07	0.44
S_{22}	−1.1900E-05	−1.1896E-05	4.0000E-09	0.03	−1.1998E-05	9.7800E-08	0.82	−1.2193E-05	2.9255E-07	2.46
C_{30}	2.5700E-05	2.5723E-05	2.3000E-08	0.09	2.5889E-05	1.8917E-07	0.74	2.5887E-05	1.8713E-07	0.73

the larger area of the solar panels if such a spacecraft configuration is selected. The spacecraft position and velocity before each flyby are initially perturbed in each direction by 1 km and 1 mm/s, respectively. Planetary orientation and ephemeris will be significantly improved as the mission progresses, and we conducted alternate simulations to verify our sensitivity to initial errors in these parameters.

To create the simulated tracking and altimetric data for each flyby, we used GEODYN II to obtain the state of the spacecraft which, when propagated with our modeling assumptions, resulted in the best match to the Europa Clipper trajectory. Along these hyperbolic paths, Doppler observables were computed at 10 s intervals, and we added Gaussian noise with an RMS computed from the Sun-Probe-Earth (SPE) angle (typically 0.06–0.11 mm/s, with a few flybys with noise greater than 1 mm/s). Altimetric ranges to the surface were computed with nadir orientation and all necessary relativistic corrections. The average measurement frequency was derived from spacecraft altitude and the altimeter performance (Figure 1b). For each crossover track, we smoothed the surface shape model in order to match its effective resolution to the laser footprint size, and we placed the crossover point randomly in the DEM grid so that the crossovers sample a variety of terrain (Figure 2b). We then added ~1 m noise to the altimetric ranges and grouped each pair of short segments around the precomputed crossover locations and times, for use in GEODYN II as a crossover measurement. The altimeter spot location was assumed to be within the beam divergence of the laser and the reconstructed knowledge of the spacecraft attitude (100 μrad).

4. Covariance Analysis

For the radio science simulation, we first performed a covariance analysis, similar to *Park et al.* [2011], but note here that the trajectory we used (13F7-A21) had been optimized, in part to provide better tidal phase sampling. Partial derivatives are computed along the truth trajectories and with no perturbation of the model parameters. The RMS of the Doppler observations is of course at noise level, and the RMS of the crossover discrepancies is ~8 m. We discarded the crossovers with large discrepancies (>100 m), which can occur due to the sampling and the local terrain (<20% of crossovers).

The least squares solution provides both adjustments (i.e., errors) and formal uncertainties. We find that the formal uncertainties from the covariance analysis are 3 to 20 times smaller than the errors. Part of the reason the formal uncertainties in the spacecraft states might be underestimated is because we do not adjust the solar radiation scale factors. Still, the covariance results (Table 2) indicate a recovery of k_2 to 0.08% (0.00022) and of h_2 to 1.5% (0.018). The low-degree gravity coefficients show errors of ~0.01% for degree 2 and ~0.1% at degree 3. The covariance analysis does not properly account for the concealed correlations and trades between parameters that do not exist around the global minimum.

5. Full Simulation

5.1. Radio Tracking Only

More realistic error estimates can be obtained with a full simulation, where POD is performed on noisy data starting from imperfect models. This is especially important in a flyby tour, where the geometry is not as robust as an orbital configuration because the dynamics are weaker (hyperbolic trajectory versus multiple short-period orbits) and long gaps exist between the flybys.

While the altimetric crossovers are a powerful measurement of the surface deformation, we found that POD should first be performed with the radiometric tracking data alone. Indeed, with large perturbations, the initial geolocation errors are such that crossovers can become degenerate due to insufficient data selection (we typically selected 50 points centered on the expected intersection, which is only a short amount of time at 128 Hz) or due to crossover discrepancies so large that they destabilize the iterative least squares process because of the inherent nonlinearity of the altimetric profiles.

To remediate this issue and realistically follow the mission scenario, we processed the radio tracking data with a batch-sequential approach, similar to *Genova et al*. [2013] with data from the MErcury Surface, Space ENvironment, GEochemistry, and Ranging (MESSENGER) mission. The first flyby is processed alone; updated arc and global parameters are used as a new a priori to process the first and second flybys, and so on. Once all 45 flybys are processed, we obtained the radio-only solution (Table 2). A few of the flybys do not contribute much to the solution, because of high radio noise due to low SPE angles. In particular, the error in the initial state of flyby #39 is very large (~7 km).

The formal uncertainties obtained were once again optimistic, by a factor of 5–20 compared to the actual errors. The errors on the degree 2 and 3 gravity coefficients (Table 2) are typically ~1% and ~10%, respectively, except for the zonal terms which are better determined. The tidal Love number k_2 is obtained to ~3% accuracy (0.0075), which would enable the definitive confirmation of the presence of a subsurface ocean. If not all the flybys are available for radio tracking, the recovery accuracy will degrade accordingly. Simulations carried out with 10 and 20 flybys indicate that the k_2 parameter can be estimated to ~16% and ~7% accuracy, respectively, consistent with the results of *Iess et al*. [2012] at Titan with Cassini. With 35 flybys, the k_2 can be recovered to similar accuracy as with the complete flyby tour.

5.2. Radio Tracking and Altimetry

To account for instrument noise and interpolation error, we weighted each crossover measurement at a nominal 10 m. Although there are fewer than 300 crossovers, this value gives significant weight to the crossovers relative to the radio data. Thus, we used the full covariance matrix of the radio-only solution to provide an a priori constraint on the initial states of each flyby when processing altimetry, to prevent spurious noise (such as topographic interpolation errors) from destabilizing the solution. We scaled each 6×6 state covariance matrix by a factor of 50 to be commensurate with the actual error level. In general, we find that the Z direction (in J2000) is the least well determined, so the states in the other two directions are not allowed to change significantly. The arc parameters and global tidal and $L = 2$ and 3 gravity coefficients are iteratively adjusted with the complete data set. The final RMS of the crossovers is ~10.3 m, higher than the covariance analysis but adequate given the tidal signal amplitude.

We found that, through the use of crossovers, the superior observation geometry of the great majority of the flybys helps better determine the states of the weaker flybys (from a radio perspective). For instance, the error in the state of flyby #39 is reduced by more than 1 order of magnitude to 500 m. The benefits of dynamics with the POD of the spacecraft for entire orbits around Jupiter would likely provide further improvement, but this is outside of the scope of this work.

The addition of altimetry also improves the gravitational parameters, in particular k_2. The error is reduced by a factor of 3, to 1% (0.0026), a level of accuracy amenable to use in interior models of Europa as has been performed on the Moon by *Williams et al.* [2014] with data from the Gravity Recovery and Interior Laboratory (GRAIL) mission.

The h_2 Love number, not measurable from radio data alone, is determined to better than 3% (0.034), which would provide some constraints on the ice shell thickness when combined with k_2. *Wahr et al*. [2006] showed that the trade-off between ice shell thickness and viscosity is largely eliminated when considering the parameter $1 + k_2 - h_2$. In our case, the error in h_2 dominates and results in a ~20 km uncertainty in ice shell thickness. Future work, such as a joint inversion of h_2 and k_2, may help reduce it. However, such a determination could provide a useful constraint in the absence of any other observation of the depth of the crust-ocean interface. A reduction in the number of flybys tracked by radio near close approach can degrade the recovery of h_2. With only 35 and 20 flybys tracked, the uncertainty in h_2 increases to ~7% and ~36%, respectively.

In order to assess the sensitivity of our results to surface roughness, we varied the amplitude of the fractal noise added to the topographic maps, either short wavelength or midwavelength, by ±50%. In some of

these cases, which are not expected from our current knowledge of Europa's topographic range [*Nimmo et al*., 2007], we found that the error in h_2 can increase, up to ~6% accuracy (0.075). We also used a DEM of Arbela Sulcus on Ganymede [*Giese et al*., 2001] instead of the Europa relief map, and we obtained very similar results (1% and 3.6% for k_2 and h_2, respectively).

We conducted another set of simulations for the case of an altimeter of limited range (1000 km). The measurement noise was increased to 10 m to reflect the larger uncertainty in geolocation. More significantly, we limited the crossovers to only those occurring when the spacecraft altitude is between 400 and 1000 km. The resulting errors in h_2 were typically of the order to 25% (~0.3), too large to significantly contribute to detailed geophysical studies.

Although we anticipate the quality of the orientation parameters of Europa to be improved by the time a mission reaches it, we performed a simulation where the right ascension (RA) and declination (DEC) of the pole position were both perturbed by 0.5° (several times the current estimated quality) [*Margot et al*., 2013]. After a sequential radio-only estimation and the addition of altimetric data, we found that the RA and DEC could be recovered to ~0.003 and ~0.02°, respectively. This is of sufficient quality to verify theoretical predictions of obliquity related to the presence of a global liquid layer, such as *Bills et al*. [2009], *Baland et al*. [2012], and *Van Hoolst et al*. [2013].

Similarly, we perturbed the Europa ephemeris by ~250 m in each direction through Set III parameters [*Brouwer and Clemence*, 1961]. These perturbations are recovered to better than 50 m, and like *Park et al*. [2011], we find that the geophysical parameters are not affected by the recovery.

6. Summary

We showed that altimetric data from a capable instrument can substantially further the geophysical objectives of the Europa Clipper mission. The global coverage enabled by its long-range capability would deliver the global shape of Europa with high accuracy, which would constrain the ice shell thickness variations and thermal loss mechanism. We conducted a comprehensive simulation with radiometric tracking and altimetric data over the 2.5 year Europa flyby tour. Compared to the radio-only case, this combination improves the estimate of the tidal Love number k_2 by a factor of 3, to $<1\%$ accuracy, makes possible a measurement of h_2, to 3–4% accuracy, and improves the overall knowledge of the spacecraft position. This demonstrates a laser altimeter on board a Europa flyby mission will strengthen and enhance the geophysical investigation.

Acknowledgments
We acknowledge the NASA support of the simulation effort by the Europa Pre-Project, through a grant to MIT. We thank F. Nimmo (UCSC) for providing the topographic models. The simulation was performed using the trajectory made available for the ICEE proposal (http://solarsystem.nasa.gov/europa/iceedocs.cfm).

The Editor thanks Giuseppe Mitri and one anonymous reviewer for their assistance in evaluating this paper.

References

Anderson, J. D., G. Schubert, R. A. Jacobson, E. L. Lau, W. B. Moore, and W. L. Sjogren (1998), Europa's differentiated internal structure: Inferences from four Galileo encounters, *Science*, *281*(5385), 2019–2022, doi:10.1126/science.281.5385.2019.

Araki, H., et al. (2009), Lunar global shape and polar topography derived from Kaguya-LALT Laser Altimetry, *Science*, *323*, 897–900, doi:19.1126/science.1164146.

Baland, R.-M., M. Yseboodt, and T. Van Hoolst (2012), Obliquity of the Galilean satellites: The influence of a global internal liquid layer, *Icarus*, *220*, 435–448, doi:10.1016/j.icarus.2012.05.020.

Bills, B. G., F. Nimmo, O. Karatekin, T. Van Hoolst, N. Rambaux, B. Levrard, and J. Laskar (2009), *Rotational Dynamics of Europa*, edited by R. Pappalardo et al., pp. 119–134, Univ. of Ariz. Press, Tucson, Ariz.

Brouwer, D., and G. M. Clemence (1961), *Methods of Celestial Mechanics*, Academic Press, New York.

Figueredo, P. H., and R. Greeley (2003), The emerging resurfacing history of Europa from pole-to-pole geologic mapping, *34th Lunar and Planetary Science Conference*, Abstract #1017.

Genova, A., L. Iess, and M. Marabucci (2013), Mercury's gravity field from the first six months of MESSENGER data, *Planet. Space Sci.*, *81*, 55–64, doi:10.1016/j.pss.2013.02.006.

Giese B., R. Wagner, G. Neukum, R. Pappalardo, J. W. Head III, and Galileo SSI Team (2001), The topography of Ganymede's Arbela Sulcus, *32nd Lunar and Planetary Science Conference*, Abstract #1743.

Head, J. W., R. T. Pappalardo, and R. Sullivan (1999), Europa: Morphological characteristics of ridges and triple bands from Galileo data (E4 and E6) and assessment of a linear diapirism model, *J. Geophys. Res.*, *104*(E10), 24,223–24,236, doi:10.1029/1998JE001011.

Hemingway, D., F. Nimmo, H. Zebker, and L. Iess (2013), A rigid and weathered ice shell on Titan, *Nature*, *500*, 550–552, doi:10.1038/nature12400.

Iess, L., N. J. Rappaport, R. A. Jacobson, P. Racioppa, D. J. Stevenson, P. Tortora, J. W. Armstrong, and S. W. Asmar (2010), Gravity field, shape, and moment of inertia of Titan, *Science*, *327*(5971), 1367–1369, doi:10.1126/science.1182583.

Iess, L., R. A. Jacobson, M. Ducci, D. J. Stevenson, J. I. Lunine, J. W. Armstrong, S. W. Asmar, P. Racioppa, N. J. Rappaport, and P. Tortora (2012), The tides of Titan, *Science*, *337*(6093), 457–459, doi:10.1126/science.1219631.

Iess, L., M. Di Benedetto, N. James, M. Mercolino, L. Simone, and P. Tortora (2014), Astra: Interdisciplinary study on enhancement of the end-to-end accuracy for spacecraft tracking techniques, *Acta Astronaut.*, *94*, 699–707, doi:10.1016/j.actaastro.2013.06.011.

Konopliv, A. S., S. W. Asmar, W. M. Folkner, O. Karatekin, D. C. Nunes, S. E. Smrekar, C. F. Yoder, and M. T. Zuber (2011), Mars high resolution gravity fields from MRO, Mars seasonal gravity, and other dynamical parameters, *Icarus*, *211*, 401–428, doi:10.1016/j.icarus.2010.10.004.

Lefèvre, A., G. Tobie, G. Chobleta, and O. Čadek (2014), Structure and dynamics of Titan's outer icy shell constrained from Cassini data, *Icarus*, *237*, 16–28, doi:10.1016/j.icarus.2014.04.006.
Lemoine, F. G., et al. (1997), The Development of the NASA GSFC and NIMA Joint Geopotential Model, Gravity, Geoid and Marine Geodesy International Association of Geodesy Symposia, 117, 461–469.
Lemoine, F. G., D. E. Smith, D. D. Rowlands, M. T. Zuber, G. A. Neumann, D. S. Chinn, and D. E. Pavlis (2001), An improved solution of the gravity field of Mars (GMM-2B) from Mars Global Surveyor, *J. Geophys. Res.*, *106*(E10), 23,359–23,376, doi:10.1029/2000JE001426.
Lemoine, F. G., et al. (2013), High-degree gravity models from GRAIL primary mission data, *J. Geophys. Res. Planets*, *118*, 1676–1698, doi:10.1002/jgre.20118.
Margot, J. L., S. Padovan, D. B. Campbell, S. J. Peale, and F. D. Ghigo (2013), Measurements of the spin states of Europa and Ganymede, European Planetary Science Congress, EPSC2013-393.
Mazarico, E., A. Genova, S. Goossens, F. G. Lemoine, G. A. Neumann, M. T. Zuber, D. E. Smith, and S. C. Solomon (2014), The gravity field, orientation and ephemeris of Mercury from MESSENGER after three years in orbit, *J. Geophys. Res. Planets*, *119*, 2417–2436, doi:10.1002/2014JE004675.
Mitri, G., R. Meriggiola, A. Hayes, A. Lefèvre, G. Tobie, A. Genova, J. I. Lunine, and H. Zebker (2014), Shape, topography, gravity anomalies and tidal deformation of Titan, *Icarus*, *236*, 169–177, doi:10.1016/j.icarus.2014.03.018.
National Research Council (2011), *Vision and Voyages for Planetary Science in the Decade 2013–2022*, The National Academies Press, Washington, D. C.
Nimmo, F., and P. M. Schenk (2008), Stereo and photoclinometric comparisons and topographic roughness of Europa, *39th Lunar and Planetary Science Conference*, Abstract #1464.
Nimmo, F., P. C. Thomas, R. T. Pappalardo, and W. B. Moore (2007), The global shape of Europa: Constraints on lateral shell thickness variations, *Icarus*, *191*, 183–192, doi:10.1016/j.icarus.2007.04.021.
Nimmo, F., B. G. Bills, and P. C. Thomas (2011), Geophysical implications of the long-wavelength topography of the Saturnian satellites, *J. Geophys. Res.*, *116*, E11001, doi:10.1029/2011JE003835.
Ojakangas, G. W., and D. J. Stevenson (1989), Thermal state of an ice shell on Europa, *Icarus*, *81*, 220–241, doi:10.1016/0019-1035(89)90052-3.
Park, R. S., S. W. Asmar, B. B. Buffington, B. Bills, S. Campagnola, P. W. Chodas, W. M. Folkner, A. S. Konopliv, and A. E. Petropoulos (2011), Detecting tides and gravity at Europa from multiple close flybys, *Geophys. Res. Lett.*, *38*, L24202, doi:10.1029/2011GL049482.
Pauer, M., S. Musiol, and D. Breuer (2010), Gravity signals on Europa from silicate shell density variations, *J. Geophys. Res.*, *115*, E12005, doi:10.1029/2010JE003595.
Preusker, F., J. Oberst, J. W. Head, T. R. Watters, M. S. Robinson, M. T. Zuber, and S. C. Solomon (2011), Stereo topographic models of Mercury after three MESSENGER flybys, *Planet. Space Sci.*, *59*, 1910–1917, doi:10.1016/j.pss.2011.07.005.
Schenk, P. M. (2009), Slope characteristics of Europa: Constraints for landers and radar sounding, *Geophys. Res. Lett.*, *36*, L15204, doi:10.1029/2009GL039062.
Scholten, F., J. Oberst, K.-D. Matz, T. Roatsch, M. Wählisch, E. J. Speyerer, and M. S. Robinson (2012), GLD100: The near-global lunar 100 m raster DTM from LROC WAC stereo image data, *J. Geophys. Res.*, *117*, E00H17, doi:10.1029/2011JE003926.
Smith, D. E., M. T. Zuber, G. A. Neumann, and F. G. Lemoine (1997), Topography of the Moon from the Clementine lidar, *J. Geophys. Res.*, *102*(E1), 1591–1611, doi:10.1029/96JE02940.
Smith, D. E., et al. (2001), Mars Orbiter Laser Altimeter: Experiment summary after the first year of global mapping of Mars, *J. Geophys. Res.*, *106*(E10), 23,689–23,722, doi:10.1029/2000JE001364.
Smith, D. E., et al. (2010), Initial observations from the Lunar Orbiter Laser Altimeter (LOLA), *Geophys. Res. Lett.*, *37*, L18204, doi:10.1029/2010GL043751.
Sotin, C., G. Tobie, J. Wahr, and W. B. McKinnon (2009), *Tides and Tidal Heating on Europa*, edited by R. Pappalardo et al., Univ. of Ariz. Space Science Series, 85-117.
Van Hoolst, T., R.-M. Baland, and A. Trinh (2013), On the librations and tides of large icy satellites, *Icarus*, *226*, 299–315, doi:10.1016/j.icarus.2013.05.036.
Wahr, J. M., M. T. Zuber, D. E. Smith, and J. I. Lunine (2006), Tides on Europa, and the thickness of Europa's icy shell, *J. Geophys. Res.*, *111*, E12005, doi:10.1029/2006JE002729.
Williams, J. G., et al. (2014), Lunar interior properties from the GRAIL mission, *J. Geophys. Res. Planets*, *119*, 1546–1578, doi:10.1002/2013JE004559.
Zuber, M. T., D. E. Smith, S. C. Solomon, D. O. Muhleman, J. W. Head, J. B. Garvin, J. B. Abshire, and J. L. Bufton (1992), The Mars Observer Laser Altimeter investigation, *J. Geophys. Res.*, *97*, 7781–7798, doi:10.1029/92JE00341.
Zuber, M. T., D. E. Smith, A. F. Cheng, and T. D. Cole (1997), The NEAR laser ranging investigation, *J. Geophys. Res.*, *102*(E10), 23,761–23,773, doi:10.1029/97JE00890.
Zuber, M. T., et al. (2012), Topography of the northern hemisphere of Mercury from MESSENGER laser altimetry, *Science*, *336*, 217–220, doi:10.1126/science.1218805.